

Perovskite Photodetector Integrated with Microfluidics for Low-Level Fluorescence Detection: Toward Self-Powered Biomarker Sensing

Md Fahim Al Fattah,[#] Asif Abdullah Khan,[#] Saikiran Khamgaonkar, Sanjana Srikant, Hesam Abouali, Md. Rasidul Islam, Aixi Pan, Mohsen Azadinia, Md. Soyaeb Hasan, Mahmoud Almadhoun, Hany Aziz, Mahla Poudineh, Vivek Maheshwari,* and Dayan Ban*



Cite This: <https://doi.org/10.1021/acsaem.4c01735>



Read Online

ACCESS |

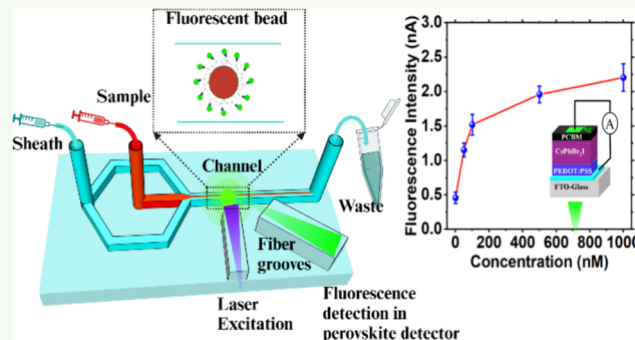
Metrics & More

Article Recommendations

Supporting Information

ABSTRACT: Inorganic (cesium) metal halide perovskites have been of extensive interest to the broader scientific community owing to their higher stability and breakthrough performance in photoelectric conversion. While substantial progress has been made in perovskite-based devices, they are increasingly attracting interest as potential candidates for fluorescent-based sensors in biological marker detection and quantification. Herein, a self-driven perovskite photodetector for fluorescence detection is reported, elucidating controlled charge carrier dynamics under the light matter interaction. The light-induced doping phenomenon, resulting from the migration of optically activated ions, generates an electric field that enables device operation without external power. However, the uncontrolled migration of those ions increases the dark current and reduces the stability of the output current. To address this, we fabricate a vertically stacked FTO/PEDOT: PSS/CsPbBr₂I/PCBM/Ag photodetector with nonsymmetrical electrode design to trigger controlled ion migration upon light illumination, thereby improving the device performance and output stability. The photodetector, driven by induced electric field due to the directional polarization, achieves an exceptionally low dark current (~298 pA), a high on/off ratio on the order of 10⁵, a responsivity of 202 mA/W, a high detectivity of 2.5×10^{11} Jones, and a fast rise and decay time (190 and 100 μ s), all are measured at 0 V, surpassing the performance of many similar state-of-the-art works. These insights are crucial for practical applications where weak light detection is required, and we demonstrate the integration of this detector with a microfluidic chip for fluorescence detection from quantum dot conjugated beads. The photodetector showcased sufficient sensitivity to detect signals from quantum dot solutions as low as ~23 nM in a microfluidic channel, highlighting the potential for future self-powered integrated platforms for biomarker sensing applications.

KEYWORDS: controlled ion migration, self-powered, photodetector, quantum dot, fluorescence, biomarker, optofluidic



INTRODUCTION

Advances in semiconductor materials design, synthesis, and characterization, coupled with novel strategies for device fabrication and integration, have led to high performance optoelectronic devices and sensors, well-suited for fluorescence detection in biological platforms.^{1–3} While Si (down to 1100 nm), Ge (800–1800 nm), GaN (200–365 nm), InGaAs (800–1700 nm), and other semiconductors dominate the ultraviolet (UV) to near-infrared (NIR) spectral detection range, they require stringent interface engineering and costly fabrication infrastructure.^{4,5} Consequently, growing interest in integrating customized optoelectronic devices with biological systems has prompted researchers to explore easily processed materials that enhance light matter interactions enabling new opportunities for sensing, diagnostic, and therapeutic.^{6,7} Hybrid organic–inorganic metal halide perovskites have

emerged as promising alternative candidates to conventional semiconductor materials in the field of optoelectronics. State-of-the-art technologies based on perovskites such as solar cells,⁸ X-ray imaging,⁹ UV–Vis photodetectors,¹⁰ photocatalysis, lasers,¹¹ and light-emitting diodes¹² have been leading the prevailing paradigm owing to their excellent photoelectric properties including high absorption coefficients, tunable bandgap, long carrier diffusion length, high carrier mobilities, excellent defect tolerance, low midgap defect

Received: September 29, 2024

Revised: December 5, 2024

Accepted: December 6, 2024

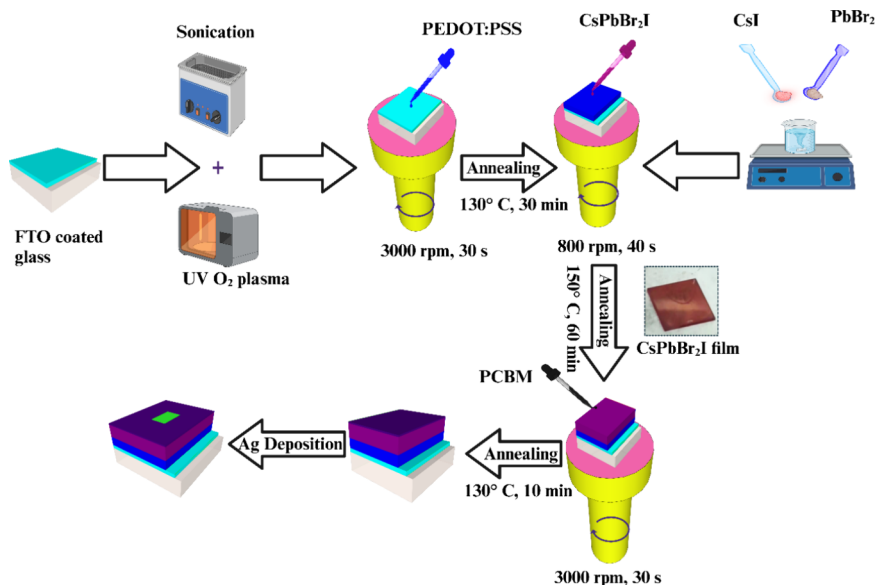


Figure 1. Schematic representation of the material synthesis and device fabrication.

densities, and so on.^{13–17} Perovskite compounds are notable for their ability to be processed from solution at low temperatures and comprise a general chemical formula of ABX₃, where A is an organic or inorganic cation, B is a metal cation, and X is a halide anion.^{18–20}

Although organic–inorganic halide perovskites have shown great promise, stability is a critical concern under light, heat, and temperature due to the volatile organic cations (MA⁺ and FA⁺), making them particularly vulnerable to degradation.^{21,22} In response to the susceptibility to stability issue, it has prompted a shift in focus toward more stable inorganic perovskites introducing Cs⁺ in place of organic cations for continued research and development. Among all inorganic perovskite materials, the widely studied CsPbBr₃ has demonstrated excellent stability even in the absence of any protective encapsulation, but a large band gap (~2.3 eV)²³ restricts the application in the visible light range. Though CsPbBr₂I and CsPbI₃ have relatively narrow band gap offering a wide absorption range, both of them suffer from poor structural stability due to low tolerance factor and are prone to thermodynamic phase transition into a nonperovskite phase which results in a reduced device performance.²⁴ On the contrary, the CsPbBr₂I compound not only presents a favorable band gap but also demonstrates exceptional stability by increasing the contents of bromide ions, making it a promising option for balanced stability and the light absorption range.^{25,26} While there have been some reports on the material characterization of CsPbBr₂I, there remains a notable lack of studies focusing on the practical application of this material, especially in self-powered photodetectors for biomedical applications. Self-powered photodetectors are indispensable for fluorescence-based biomarker detection, driving the miniaturization of point-of-care diagnostic devices while ensuring energy efficiency, portability, and seamless integration for accessible and reliable healthcare solutions.

In light of this, the unique intrinsic properties of CsPbBr₂I offer a promising pathway to achieve self-powered operation utilizing ionic conduction to induce an internal electric field for efficient charge separation without the need for external power. Of particular interest, ion migration is speculated to be the

origin of the contributing factor to generating the built-in electric field by forming *p*–*i*–*n* or *n*–*i*–*p* doped structure within the absorbing material, which can be triggered by external electrical poling or light-induced poling as proved by many experimental evidence.^{27–30} However, the doping effect, resulting from the accumulation of charged ions triggered by external electrical poling, profoundly impacts structural and morphological degradation, especially at high-voltage poling. Most importantly, the back diffusion of ions in the absence of an externally applied electric field could eventually nullify the doping effect within a few days.²⁸ On the other hand, light-induced polarization optically activates the ions within the material, leading to the formation of an electric field which is comparable to the electrical poling. This approach eliminates the need for external electrical manipulation. However, the role of ion migration in perovskite photodetectors has been a topic of considerable debate, with studies citing it as both a beneficial and a detrimental factor for device performance. While uncontrolled ion migration is linked to increased dark current and reduced stability, controlled or directional ion migration can significantly enhance device performance. In this work, we leverage the nonsymmetrical electrode design of FTO/PEDOT: PSS/CsPbBr₂I/PCBM/Ag photodetector to induce controlled ion migration within the CsPbBr₂I absorber layer under light stimulation, realizing the full potential of this detector in self-powered mode. By exploiting the controlled light-induced electric field as the driving force, the photodetector exhibits extremely low dark current (~298 pA), a high on/off ratio on the order of 10⁵, a decent responsivity of 202 mA/W, high detectivity of 2.5×10^{11} Jones, high bandwidth of 3.1 kHz, and fast response time (190 μs/100 μs) at 0 V which is better than those of previously reported similar kind photodiodes. Furthermore, the device was found to be very stable after around 1 month of direct exposure to air. These exceptional performances motivate us to employ this detector for applications where weak signal detection is critical, such as in fluorescently tagged biomarker detection. To demonstrate its practical application, we integrated this photodetector with a microfluidic channel for quantum dot tagged microparticle detection as a proof of concept, which could facilitate further

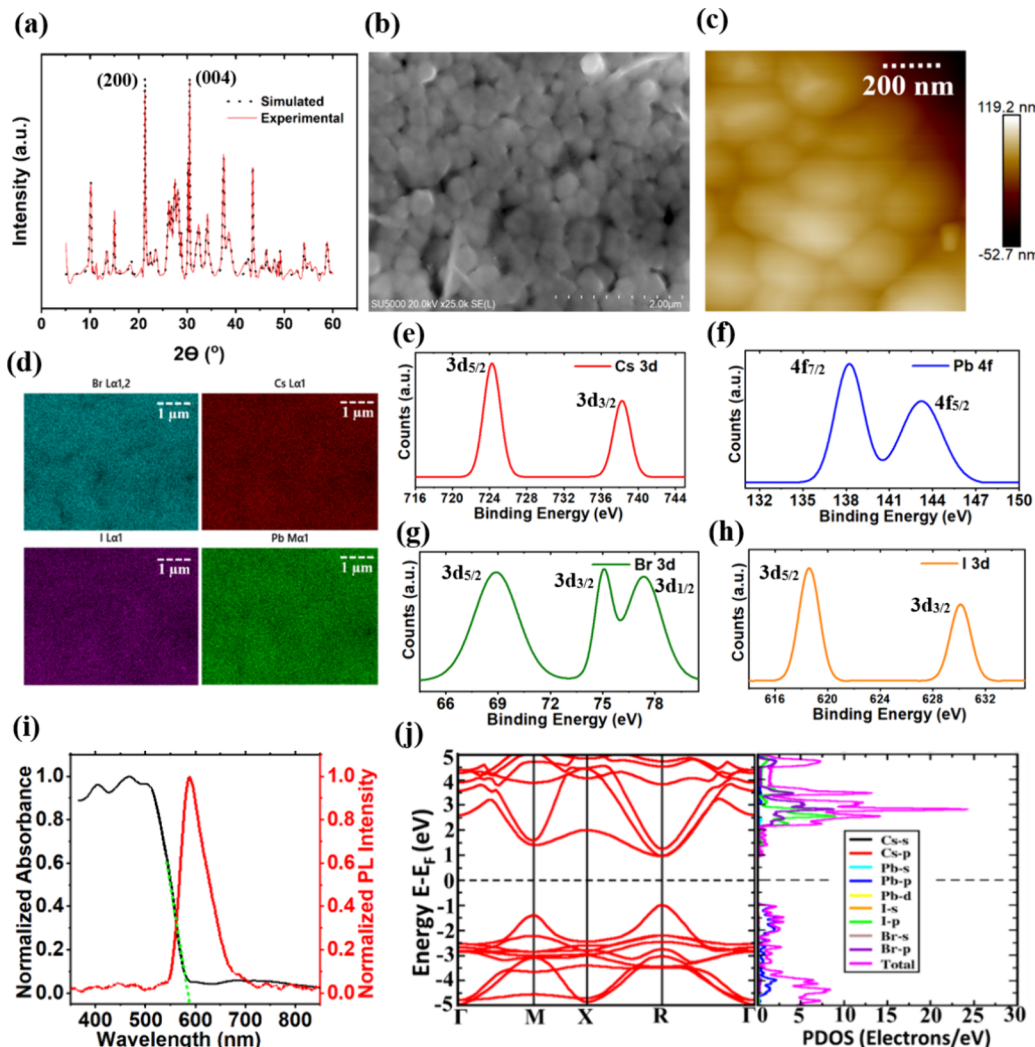


Figure 2. Material design and characterization. (a) XRD pattern of CsPbBr_2I crystal. (b) SEM image showing the surface morphology of the CsPbBr_2I thin film. (c) AFM image of CsPbBr_2I grains on the surface. (d) EDS mapping of the constitutive elements of Cs, Pb, Br, and I. (e–h) XPS spectra showing valence states of Cs 3d, Pb 4f, Br 3d, and I 3d, respectively. (i) Absorption and PL spectra of CsPbBr_2I film. (j) Simulated band structure.

research to monitor blood glucose, insulin, or lactate levels within an integrated self-powered biological platform.

EXPERIMENTAL SECTION

Photodetector Fabrication. Materials. Materials include cesium iodide, CsI ($\geq 99.99\%$ trace metals, Sigma-Aldrich); lead bromide, PbBr_2 ($\geq 98\%$, Sigma-Aldrich); poly(3,4-ethylenedioxythiophene) polystyrenesulfonate, PEDOT: PSS (Sigma-Aldrich); [6,6]-phenyl-C₆₁-butyric acid methyl ester, PCBM ($\geq 99.9\%$, Xi'an polymer light technology Corp.); dichloromethane (99.9% , Sigma-Aldrich); and dimethylformamide ($\geq 99\%$, Sigma-Aldrich).

Methods. Fluorine-doped tin oxide (FTO) coated glass substrate is ultrasonically cleaned for 15 min with acetone, isopropanol (IPA), and deionized (DI) water. Then, we performed oxygen plasma treatment on the surface of the substrate for 15 min. To synthesize the CsPbBr_2I precursor, we used an equimolar (1 mmol: 1 mmol) amount of CsI, and PbBr_2 in DMF, and vigorously mixed them for 12 h at 60 °C. The mass ratio of the solution was kept at 35 wt %. The device was fabricated by the following steps: first, PEDOT: PSS solution was spin-coated on the FTO/glass at 3000 rpm for 30 s and cured at 130 °C for 30 min. Second, CsPbBr_2I solution was spin-coated onto the PEDOT: PSS layer at 800 rpm for 40 s followed by antisolvent treatment. The film was cured at 100 °C for 45 min followed by annealing at 150 °C for 1 h. Third, the PCBM solution

was spin-coated on the CsPbBr_2I layer at 3000 rpm for 30 s, followed by annealing at 130 °C for 10 min. Finally, a 50–100 nm silver layer was sputtered on the PCBM using a shadow mask as the top electrode for the device. A complete process flow of the material synthesis and the device fabrication is shown in Figure 1.

Material and Device Characterization. X-ray diffraction (XRD) patterns of the perovskite powder were collected by using a Bruker D8-Discover diffractometer with Cu K α radiation ($\lambda = 1.5418 \text{ \AA}$). The surface morphology and elemental distribution on the film (CsPbBr_2I) were characterized by a field-emission scanning electron microscope (FE-SEM, Hitachi-SU 5000) fitted with X-ray energy dispersive spectroscopy (EDS). The surface roughness was measured by Bruker atomic force microscope (AFM, Dimension Icon). The X-ray photoelectron spectroscopy (XPS, VGS ESCA Lab 250 Imaging ESCA) experiment was performed in a UHV multipurpose surface analysis system operated at base pressures of $< 10^{-9} \text{ mbar}$. Optical absorption and the photoluminescence spectra were collected by a UV spectrometer (UV-2501PC, Shimadzu) and Horiba Fluorolog Time Correlated Single Photon Counting system, respectively. The band structure was simulated using Quantum Expresso software. The steady-state I – V measurement of the detector was performed by Keithley 2354B using a light source of 488 nm (Model: LP488-SF20G, Thorlabs). Digilent analog discovery 3 oscilloscope module was used for modulating the 488 nm laser at different frequencies for

the time-dependent response measurement at different light intensities.

Biological Sample, Microfluidic Chip, and Optofluidic Integration. *Assay Details: Materials and Methods.* Carbodiimide-mediated covalent coupling was used to functionalize the surface of magnetic beads with increasing concentrations of streptavidin 525 Quantum Dots (Qdots) to validate the optical system. 15 μm carboxyl modified magnetic beads were purchased from Spherotech, Inc. Streptavidin-conjugated 525 QDots were purchased from ThermoFisher. All reagents for covalent coupling and buffer preparation were purchased from Sigma-Aldrich. 10 mg of EDC (1-ethyl-3-(3-(dimethylamino)propyl) carbodiimide hydrochloride) and 10 mg of NHS (*N*-Hydroxy succinimide) were dissolved in pH 5.2 0.1 M (2-(*N*-Morpholino) ethanesulfonic acid) MES buffer and labeled as coupling solution. 10⁵ beads were aliquoted into each sample and washed twice and resuspended in 500 μL of coupling solution, followed by a room temperature incubation with shaking for 15 min. Beads were then washed again and resuspended in pH 7.5 MES buffer with varying concentrations of streptavidin-Quantum dot 525 solution. These were incubated at room temperature for 1–2 h with shaking before final wash steps and optical characterization. All samples were resuspended in ultrapure water at final volumes of 500 μL . Four concentrations of QDot coverage were tested, namely, 50, 100, 500, and 1000 nM. Negative controls were beads without any surface modifications. All samples were characterized with flow cytometry for further validation.

Microfluidic Chip Fabrication. The microfluidic device design and the microscopic image of the channel are shown in Figure S1 in the Supporting Information. The device includes one main channel of size 500 $\mu\text{m} \times 500 \mu\text{m}$. There are two grooves of 250 and 450 μm for the excitation and emission optical fiber insertion, respectively. The mold for the devices was designed by CAD software (SolidWorks, Dassault Systems), and it was fabricated through the stereolithography 3D printing (SLA) method (Formlabs Form 3B+). Following the mold fabrication, the microfluidic devices were fabricated through poly(dimethylsiloxane) (PDMS) casting. PDMS (SYLGARD 184 Silicone Elastomer Kit, Dow Corning) was cast on the mold and baked for 4 h. The prepared PDMS part of the device was bonded to a cleaned glass substrate using a plasma etcher (15 W, 30 s, 10 sccm, air; Tergeo Plasma Cleaner, Pie Scientific). The fabricated PDMS devices were degassed for an hour before their use by a nonionic surfactant, Pluronic F108 (Sigma-Aldrich).

Integrated Optofluidic Setup. In this section, we integrated the perovskite photodetector with a microfluidic chip for fluorescence detection by exciting quantum dot-tagged channel bound beads. The integrated experimental setup is depicted in Figure S2 in the Supporting Information. A pump was used to inject the sample through the channel. The flow rate of the sample was 30 $\mu\text{L}/\text{min}$. A multimode optical fiber (200 μm core diameter, Model: M137L02, Thorlabs) having a numerical aperture of 0.22 coupled with a 405 nm Laser (Model: LP405-MF300, Thorlabs) was placed inside the grooves of the microfluidic chip to provide the excitation energy to the moving beads. Another multimode optical fiber having a numerical aperture of 0.39 (425 μm core diameter, Model: M118L02, NA: 0.39, Thorlabs) was placed at a 45° angle with the excitation for collecting the fluorescence from the quantum dot-tagged beads. The fluorescence light was then passed through a bandpass filter, 520/10 nm (Model: FBH520–10, Thorlabs), while rejecting all other background light. After that, a 9 mm focusing lens (Model: LB1494-A, Thorlabs) was used to focus the beam at the active area of the perovskite detector. The detector output was amplified by using a preamplifier (Model: SR570, Stanford Research System), and a USB oscilloscope from Digilent was interfaced with a computer for data collection and processing.

RESULTS AND DISCUSSION

Material Design and Characterization. X-ray diffraction was used to examine the crystal structure of the CsPbBr₂I thin film, as shown in Figure 2a. The sharp and high intensity of the

XRD peaks corroborates the excellent crystallinity of the CsPbBr₂I thin film. The dominant peaks are corresponding to the (200) and (004) planes at 21.28° and 30.18°, respectively. At room temperature, CsPbBr₂I possesses an orthorhombic structure with the calculated lattice constants of $a = 8.386 \text{ \AA}$, $b = 8.18 \text{ \AA}$, and $c = 11.835 \text{ \AA}$, according to the $((d_{hkl})^{-2} = h^2/a^2 + k^2/b^2 + l^2/c^2)$, where a , b , and c are the lattice constants; d is the lattice spacing; and h , k , and l are the Miller indices. The calculated lattice parameters exhibit a deviation in the b/a ratio from the standard orthorhombic value of 1.005–0.975 due to lattice distortion. Considering the fact that iodine has a higher ionic radius than bromine atoms, their relative positions in the octahedra will likely stretch the crystal lattice.³¹ This may create larger polarization and dipole moments in the crystal than in the standard CsPbBr₃ system and is conducive to more efficient photocarrier separation.

To observe the surface morphologies, we examined individual grains of the films by SEM and AFM. Figure 2b shows a scanning electron microscope (SEM) image of the CsPbBr₂I film. From the film surface, perovskite grains with an average size of 200–400 nm are visible. Large grains with less grain boundaries are crucial for long carrier diffusion length. The grains as observed from the SEM image in Figure 2b were also examined by the atomic force microscope, as shown in Figure 2c. Large grains with an average size of 200–400 nm were clearly visible in the AFM surface topography image. The elemental distribution in CsPbBr₂I was mapped by using SEM energy dispersive spectroscopy (EDS), as shown in Figure 2d. We observed a homogeneous distribution of Cs, Pb, Br, and I atoms in the perovskite film verifying structural integrity. From the EDS spectrum in Figure S3, we estimated the elemental composition, which matches well with the calculated ones.

We performed X-ray photoelectron spectroscopy to get the information on valence states in CsPbBr₂I, as shown in Figure 2e–h. For the cesium atoms, two 3d peaks were found at binding energies of 738.2 eV (3d_{3/2}) and 724.2 eV (3d_{5/2}). The peaks for Pb 4f were at 143.2 eV (4f_{5/2}) and 138.2 eV (4f_{7/2}). The bromine and iodine peaks were at the binding energies of 77.3 eV (Br 3d_{1/2}), 75 eV (Br 3d_{3/2}), 69.1 eV (Br 3d_{5/2}), 630.1 eV (I 3d_{3/2}), and 618.6 eV (I 3d_{5/2}), respectively. It should be noted that, depending on the relative position of Br and I atoms, lattice distortion will change the atomic interaction environment; hence, a slight shift in the binding energies could be found.

To find the suitable photon detection range of CsPbBr₂I, the absorption and the photoluminescence (PL) spectra were collected, as shown in Figure 2i. The absorption spectrum underscores the optical properties of the absorbing layer across the visible light wavelength, where it was noticed that the absorption edge starts to rise from 589 nm extending toward a wavelength shorter than 400 nm. The optical band gap was calculated to be 2.1 eV from the Tauc plot of the measured absorption spectrum, as shown in Figure S4 following the Kubelka–Munk equation:

$$(\alpha h\nu)^2 = A(h\nu - E_g) \quad (1)$$

where α is the absorption coefficient and $h\nu$ is the incident light energy. The steady state PL spectrum as shown in Figure 2i exhibits an emission peak at the wavelength of 587 nm, which is consistent with the sharp edge of the UV-Vis absorption spectrum. Furthermore, density functional theory (DFT) calculation shows that the material exhibits a direct

band gap of 1.96 eV, a result that closely aligns with our experimental data, thereby validating our findings. The small discrepancy between simulated and experimental results primarily arises because DFT often underestimates band gaps due to its approximation of exchange–correlation energy, which inadequately accounts for electron–electron interactions.^{32–34} The calculated band structure and the partial density of states (pDOS) depicted in Figure 2j suggest that the electronic structure near the Fermi level originally stems from Pb 5p and Br 4p states.

Device Design, Fabrication, and Characterization.

With a comprehensive understanding of the material properties, we now focus on the utilization of this material within the device structure, as shown in Figure 3a. The photodetector was

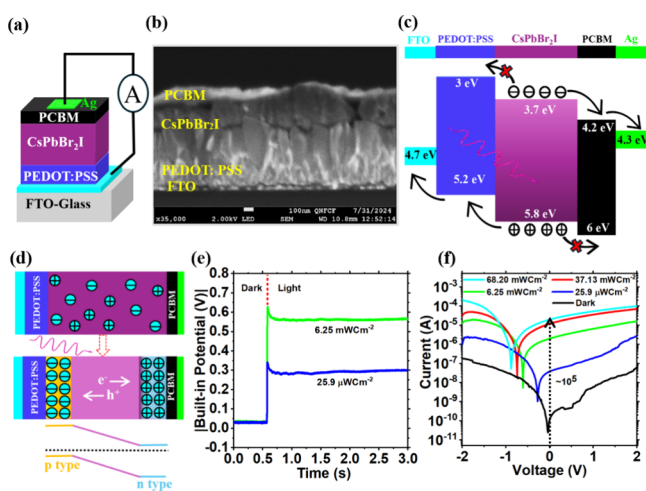


Figure 3. Device structure, working principle, light-stimulated polarization, and self-powered operation. (a) Device structure. (b) Cross-sectional SEM image showing the multilayered configuration. (c) Schematic energy band diagram. (d) Light-induced poling. (e) Built-in potential and open circuit voltage under dark and light illumination respectively. (f) I – V characteristics at different intensities of light illumination.

fabricated by a vertically stacked configuration where the CsPbBr_2I thin film was employed as a visible light absorber between the PEDOT: PSS and PCBM layers. The p-type PEDOT: PSS was used to transport the photogenerated holes, while the PCBM was used to transport the electrons. FTO and Ag were used as the electrode to collect the e-h pairs to be circulated in the external circuit. The thickness of each layer was determined from the cross-sectional SEM image of the device, as shown in Figure 3b. The approximate thickness for FTO, PEDOT: PSS, CsPbBr_2I , and PCBM layer was found to be 70, 200, 400–500, and 90 nm, respectively. We explain the operation of the photodetector by the energy level diagram of each of the layers, as shown in Figure 3c. When the detector is illuminated, the light passes through the transparent FTO and is then absorbed in the perovskite layer, generating e-h pairs to circulate photocurrents in the external circuit without applying any bias. In our design, the work function difference of each of the layers was matched in such a way as to allow electrons and holes to transit through PCBM to the Ag electrode and PEDOT: PSS to the FTO electrode, respectively, while they face a barrier to flow in the opposite direction.

Now, the carrier dynamics within the device under illumination was thoroughly investigated to realize the origin of self-powered phenomena. The light-stimulated poling effect within the perovskite material was utilized as the sole contributing factor to the device operating without any external power. The controlled poling of the stimulated ions can only be triggered if there is a present V_{bi} within the as-prepared device. Here, the initial V_{bi} generated due to the resultant effect of the device nonsymmetry which is too small to offer reasonable photovoltaic performance but very important to initiate the light-induced poling. This V_{bi} acts not only on the photocarrier extraction but also on all the electrically charged entities, thus facilitates the ions to accumulate at the interfaces, as these interfaces are ionically blocking. When the device is illuminated, the optically activated positive ions and negative ions within the CsPbBr_2I perovskite layer are driven toward the PCBM/Ag and PEDOT: PSS/FTO electrode, respectively, causing a space charge region to enhance the n-type and p-type doping concentration, as illustrated in Figure 3d. The accumulated space charge region in the perovskite layer increases the band bending, thus resulting an enhanced electric field to drive the photogenerated carrier effectively to the external circuit. The open circuit voltage was measured under dark and different intensities of light illumination, as shown in Figure 3e. The magnitude of the built-in potential or open circuit voltage (V_{oc}) under dark condition was found to be 0.035 V, which remains constant over time. The V_{oc} climbed rapidly from 0.035 to 0.35 V and 0.65 V under illumination of $25.9 \mu\text{W}/\text{cm}^2$ and $6.25 \text{ mW}/\text{cm}^2$ optical power density which is sufficient for providing the driving force to separate e-h pairs. Immediately after the light illumination, the V_{oc} value was observed to be decreased by the amount of V_{bi} due to their opposite working direction, and it saturates when the drift and reverse diffusion of ions reach equilibrium. The light-stimulated potential enhanced by the controlled polarization of ions as demonstrated in Figure 3d,e is clearly visible in the I – V characteristics in Figure 3f measured in dark and different optical power densities. To avoid the hysteresis caused due to the low voltage poling when scanning for I – V curves, the measurements were delayed 2–3 min after one intensity to another. It should be noted that the lowest dark current does not occur at zero bias which aligns with the observation that a small external bias is required to compensate the V_{bi} (V_{oc}) under dark. Therefore, the actual dark current at which the device will be operating (0 V) is slightly higher than the minimum dark current shown by an arrow pointing upward intersecting the black curve, as shown in Figure 3f. The dark current was measured to be very low on the order of pA ($\sim 298 \text{ pA}$) at 0 V which is attributed to the highly uniform thin film, as confirmed by the SEM and AFM results, as shown in Figure 2b,c. Additionally, reduced bulk defects as the optically activated ions are driven away from the active area of the perovskite material to the electrodes is another major contributing factor for such a low dark current. The photocurrent shows a sharp increase as the excitation light intensity increases. The shift in the minimum point of the photocurrent toward the left as the intensity increases signifies the increase in potential induced by light illumination. Since the dark current increases drastically with the increase of external voltage and we are interested in operating the device at 0 V, the contrast in dark current and photocurrent at zero bias is more important. Our photodetector operated at zero bias shows a remarkable on/off ratio

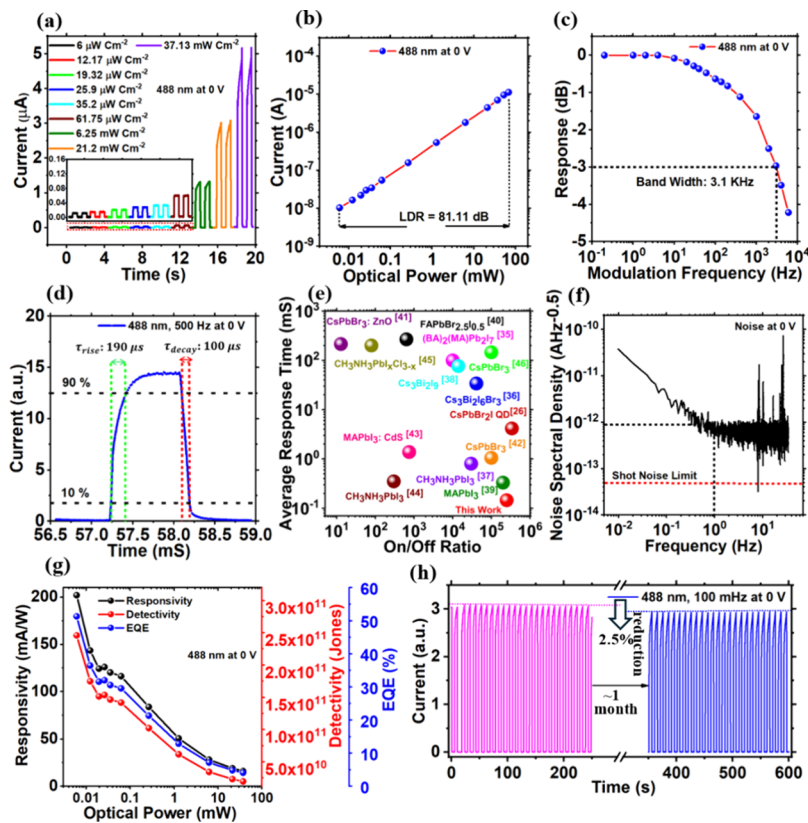


Figure 4. Performance evaluation and long-term stability testing. (a) Time-dependent photocurrent response at various light intensities. (b) Current vs optical power to determine the LDR. (c) Bandwidth. (d) Time-resolved photocurrent response for rise and decay time determination. (e) Average response time and on/off ratio comparison. (f) Noise spectrum of the device. (g) Responsivity, detectivity, and EQE with respect to optical power. (h) Long-term stability test of the photodetector.

on the order of 10^5 due to the highest contrast between dark and photo current as indicated by an upward black arrow intersecting a cyan curve.

Following the analysis of the I - V curve at different light intensities, Figure 4a provides further insight into the device's photocurrent response over time under varying illumination intensities. As shown, the current increases consistently with the incident light intensity, ranging from $6 \mu\text{W}/\text{cm}^2$ to $37.13 \text{mW}/\text{cm}^2$. The inset further illustrates the device's sensitivity and responsiveness in the lower intensity region, confirming its ability to operate effectively even under minimal illumination without any bias. However, when a bias is applied, the device's output becomes unstable and fluctuates due to the perturbation to the equilibrium of ion distribution caused by the external electric field. The Supporting Information (Figure S5) provides a detailed comparison of the current responses under positive (+2 V), negative (-2 V), and zero (0 V) biases. The instability observed under both positive and negative biases underscores the critical role of ion dynamics. Recognizing this instability due to external perturbation to the light-induced electric field, we conducted all subsequent measurements at 0 V without disrupting the equilibrium to ensure reliable and consistent results.

Now, we studied the dependency of photocurrent on the incident optical power in Figure 4b which clearly shows the linear behavior of photocurrent as the optical power increases from $6 \mu\text{W}$ to 68.2mW . Their relation can fairly be assessed by the power law eq 2 as follows:

$$I_{\text{photo}} = P_{\text{optical}}^\alpha \quad (2)$$

where I_{photo} is the photocurrent, P_{optical} is the incident optical power, and α is the exponent power index that determines the response of photocurrent to excitation light. The value of α was determined to be 0.8 a slight deviation from the ideal value 1, suggests a high charge collection efficiency where most of the carriers swept out to the external circuit before they recombine. The linear dynamic range (LDR) defines the optical power margin within which the photocurrent increases linearly with the increase of the incident optical power and can be estimated by eq 3.

$$\text{LDR} = 20 \times \log \frac{P_{\text{optical-max}}}{P_{\text{optical-min}}} \quad (3)$$

where $P_{\text{optical-max}}$ and $P_{\text{optical-min}}$ are the maximum and minimum optical power within the linear range. A large LDR value of 81.11 dB was observed, as indicated in Figure 4b. Figure 4c depicts the response speed that determines the capability of the photodetector to follow a rapidly changing signal. This measurement was performed by collecting the output current at 0 V when excited with a 488 nm laser diode modulating at different frequencies. The -3 dB frequency at which the output current declined to 70.7% of its maximum value was found to be 3.1 kHz, as indicated in Figure 4c. The response time of the photodetector is calculated to be $112.9 \mu\text{s}$ according to the formula $f_{-3\text{dB}} = 0.35/\tau$, where τ is the average response time of the rise and decay time, which is almost consistent with the response time measured in Figure 4d. A single cycle of the photocurrent is plotted in Figure 4d excited with a 500 Hz modulating signal from which the rise time and

Table 1. Comparative Analysis of Key Performance Parameters of Perovskite-Based Photodetectors

material	bias (V)	LDR (dB)	responsivity (mA/W)	detectivity (Jones)	on/off ratio	response time (ms)	ref
(BA) ₂ (MA)Pb ₂ I ₇	5	89		1 × 10 ¹¹	10 ³	125/74	35
Cs ₃ Bi ₂ I ₄ Br ₃	0		15	4.6 × 10 ¹¹	4.1 × 10 ⁴	40.7/27.1	36
CH ₃ NH ₃ PbI ₃	0				3 × 10 ⁴	0.85/0.75	37
Cs ₃ Bi ₂ I ₉	1		3.8	1.6 × 10 ¹²	1.4 × 10 ⁴	62.74/90.25	38
MAPbI ₃	0	107	260	7.01 × 10 ¹¹	2 × 10 ⁵	0.08/0.58	39
MAPbI ₃	0	140	230	1.27 × 10 ¹¹		0.014/0.002	47
FAPbBr _{2.5} I _{0.5}	0	85	59.89	4.95 × 10 ¹⁰	636	202/331	40
CsPbBr ₃ :ZnO	0		11.5		12.86	409/17.92	41
CsPbBr ₃	3	100	6 × 10 ⁶	~10 ¹³	10 ⁵	0.5/1.6	42
MAPbI ₃ : CdS	0		480	2.1 × 10 ¹³	750	0.54/2.21	43
CH ₃ NH ₃ PbI ₃	10		100	1.02 × 10 ¹²	300	0.3/0.4	44
CH ₃ NH ₃ PbI _x Cl _{3-x}	0/0.6		926.1	1.2 × 10 ¹¹	79.1	<200/200	45
CsPbBr ₃	0		28	1.7 × 10 ¹¹	10 ⁵	230/60	46
CsPbBr ₃ :P3HT	0	128.59	1400	6.59 × 10 ¹⁴	10 ⁵	152/156	48
CsSnBr ₃ :P3HT	0	~133	1560	1.40 × 10 ¹⁴	5.88 × 10 ⁵	279/171	49
PbS:CsSnBr ₃	-1		4.32 × 10 ⁶	2.7 × 10 ¹⁵	10 ⁶	631/452	50
PbSe:CsPbBr _{1.5} I _{1.5}	0	91	6160	5.96 × 10 ¹³	10 ⁵	350/375	51
CsPbBr ₂ I QD	0		375	1.12 × 10 ¹³	3.44 × 10 ⁵	3.8/4.5	26
CsPbBr ₂ I	0	81.1	202	2.5 × 10 ¹¹	2 × 10 ⁵	0.19/0.1	this work

decay time can be extracted. It is important to highlight that the rise time refers to the duration for the photocurrent to transition between 10% and 90% of its peak value and vice versa. Based on this criterion, τ_{rise} is calculated to be 190 μs , while τ_{decay} is estimated to be 100 μs . Figure 4e compares the average response time and the on/off ratio for self-powered perovskite-based photodetector, indicating that our as-fabricated CsPbBr₂I photodetector in this work shows the fastest response time and the highest on/off ratio with other state-of-the-art PDs.^{26,35–46}

Two other essential figures-of-merit for evaluating the performance of a self-powered photodetector are its responsivity (R), which measures its ability to convert incident light into electrical signals, and external quantum efficiency (EQE), representing the efficiency of photon-to-electron conversion within the device. The responsivity, R , and the EQE can be defined and calculated using the following two equations:

$$R[\text{AW}^{-1}] = \frac{I_{\text{photo}} - I_{\text{dark}}}{P_{\text{optical}} \times A} \quad (4)$$

$$\text{EQE}[\%] = R \times \frac{h \times c}{e \times \lambda} \times 100 \quad (5)$$

where I_{dark} is the dark current, A is the effective illumination area of the detector, h is the Planck constant, c is the velocity of light, λ is the wavelength of the incident light, and e is the charge of electron. Accordingly, the R and the EQE are plotted in Figure 4g at zero external bias, keeping the excitation wavelength fixed at 488 nm. Both the R and the EQE responses were found to be increased as the illuminated optical power decreased which is crucial for weak light detection. At higher optical powers, while more charge carriers are generated, the likelihood of recombination increases due to higher carrier density, leading to a reduction in R and EQE. Additionally, the filling of trap states further contributes to this decreased trend, as this limits the number of free carriers available. Thermal effects at higher optical powers may also enhance nonradiative recombination, further diminishing the responsivity and efficiency of the photodetector. However, at

the lowest measured level of incident light intensity, the highest values for R and EQE were extracted from Figure 4g as 202 mA/W and 53%, respectively.

The detectivity (D^*), another key figure-of-merit, is determined by the responsivity and the noise of a photodetector according to the following equations:

$$D^*[\text{cmHz}^{-1/2}\text{W}^{-1} \text{ or Jones}] = \frac{\sqrt{A \times \Delta f}}{\text{NEP}} = \frac{R}{I_{\text{noise}}} \times \sqrt{A \times \Delta f} \quad (6)$$

$$\text{NEP}[\text{AHz}^{-1/2}] = \frac{I_{\text{noise}}}{R} \quad (7)$$

$$I_{\text{noise}} = \sqrt{(I_{1/f})^2 + (I_{\text{shot}})^2 + (I_{\text{thermal}})^2} \quad (8)$$

$$I_{\text{shot}} = \sqrt{2 \times e \times I_{\text{dark}}} \quad (9)$$

$$I_{\text{thermal}} = \sqrt{\frac{4 \times K_B \times T \times \Delta f}{R_{\text{resistance}}}} \quad (10)$$

where NEP is the noise equivalent power; Δf is the electrical measurement bandwidth; I_{noise} is the total noise current; I_{shot} and I_{thermal} are the shot and thermal noise, respectively; $I_{1/f}$ is low frequency noise; K_B is the Boltzmann constant; T is the temperature; and $R_{\text{resistance}}$ is the resistance of the device.

Typically, the noise current depends on the device dark current, which is low if the dark current is low. If the noise current is mainly contributed by the shot noise, it can readily be derived using eq 9 from the dark current. However, in numerous scenarios, intrinsic noise may be altered by charge defects within the materials. Frequency-dependent noise current is commonly attributed to carrier trapping and detrapping, often surpassing shot noise level as marked in Figure 4f with a red horizontal dashed line. Hence, accurately assessing noise levels requires direct measurement from the device rather than just calculation from the dark current. Here,

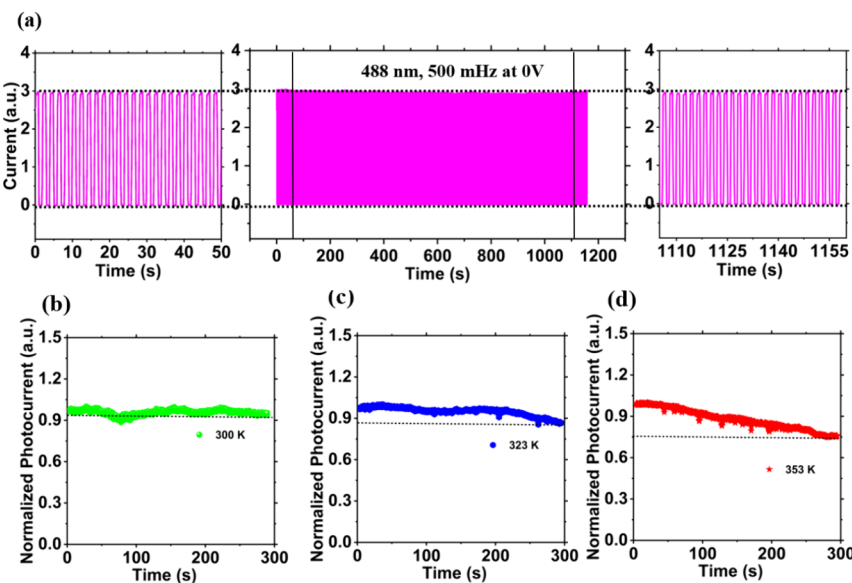


Figure 5. (a) Continuous track of the photocurrent at 0 V over an extended period (1200 s, 600 cycles). Normalized photocurrent without any encapsulation over time at (b) 300 K, (c) 323 K, and (d) 353 K.

in this study, a fast Fourier transform was performed on the time-dependent dark current collected at 0 V to obtain the total noise current, as shown in Figure 4f. It shows that the total noise current measured with this photodetector is only $\sim 10^{-12}$ $\text{AHz}^{-1/2}$. Based on the responsivity of the CsPbBr_2I photodetector, the highest detectivity (D^*) value is estimated to be approximately 2.5×10^{11} Jones, as illustrated in Figure 4g. Table 1 compares all of the performance metrics of the reported perovskite photodetector in this work with other similar published works in the literature. Finally, the device's stability was assessed by measuring the output current by providing a 100 mHz modulated optical signal for 250 s at 0 V. As depicted in Figure 4h, the device demonstrates outstanding repeatability and long-term storage stability. Even after being stored in air and moisture for around 1 month, the output current of the device decreased by only 2.5%, keeping the excitation conditions constant. Furthermore, the unencapsulated device was tested under repeated illumination for 600 cycles (500 mHz modulated signal for 1200 s), as shown in Figure 5a, where the photocurrent remained stable, indicating excellent operational stability under extended use. However, in practical applications, photodetectors are often required to operate under varying and sometimes harsh environmental conditions, including elevated temperatures. To evaluate the thermal stability of the proposed CsPbBr_2I photodetector, temperature-dependent photocurrent measurements were performed under controlled conditions. The device was mounted on a heating plate, and the temperature was externally adjusted to 300, 323, and 353 K, with all other testing conditions remaining unchanged for comparison. As shown in Figure 5b, at 300 K (room temperature), the photocurrent remained highly stable with negligible fluctuations over the testing period of 300 s, demonstrating the intrinsic stability of the CsPbBr_2I material under ambient conditions. At a moderately elevated temperature of 323 K, a slight decline in photocurrent was observed over time, as shown in Figure 5c, indicating minor thermal effects. When the temperature was further increased to 353 K in Figure 5d, a more pronounced decrease in the photocurrent was recorded, stabilizing at approximately 75% of the initial value. This

reduction is attributed to the thermally induced migration of ions and the generation of structural defects, which lead to increased carrier trapping and a subsequent decrease in photocurrent. These results suggest that the CsPbBr_2I photodetector exhibits excellent stability at room temperature and moderate thermal conditions.

Quantum dot Tagged Microparticle Detection for Biomedical Application. The CsPbBr_2I perovskite-based photodetector's responsivity and detectivity trend make it ideally suited for detecting weak fluorescence signals emitted by quantum dots tagged beads within microfluidic channel. The practical feasibility of this high-performance and stable perovskite detector was demonstrated by integration with a microfluidic chip for fluorescence detection. Generally, a large microscope equipped with a CCD camera is used for fluorescently activated biomarker detection which is typically bulky, costly, and requires alignment and calibration, limiting their suitability and portability in every healthcare unit especially in rural areas.^{52–54} Additionally, commercial silicon-based detectors, despite their widespread use in fluorescence detection,^{55–57} are expensive and involve complex fabrication processes, making them less practical for widespread adoption. Herein, we designed an experiment to determine the capability of this perovskite detector of resolving fluorescence signal from different concentrations of quantum dots solution. Figure 6a depicts the functionalization of beads coated with quantum dots and its excitation–emission spectra. Based on the absorption spectrum of the active perovskite material, 525 nm Qdots having concentrations of 0, 50, 100, 500, and 1000 nM were chosen for the experiment. Details about the sample preparation are provided in the experimental section. The integration of the detector with microfluidic chip is illustrated in Figure 6b. The sample injected through the channel exposed with 405 nm laser light emits fluorescence at a 525 nm wavelength. An optical fiber collects the fluorescence light, passes through a 520/10 nm band-pass filter, and then focuses onto the active area of the detector by using a focusing lens. The output current of the detector, which is proportional to the incident fluorescence light, is amplified by a current preamplifier. The amplifier output is then recorded by

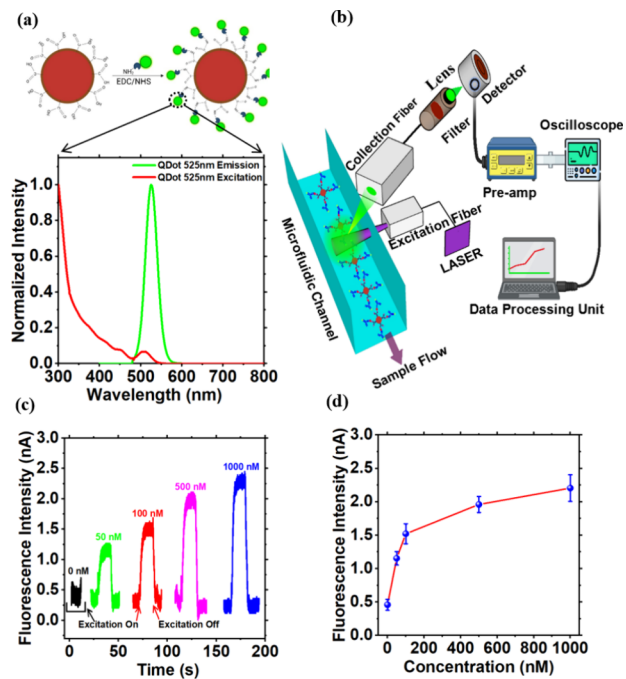


Figure 6. Integrated Optofluidic platform for fluorescence detection. (a) Process flow for the bead functionalization with quantum dots with the excitation and emission spectra for 525 nm QDots. (b) Integration of the perovskite photodetector with microfluidic channel for fluorescence detection. (c) Time-dependent fluorescence intensity at different concentrations for 525 nm QDots. (d) Calibration curve.

connecting a USB oscilloscope to the data processing unit. Figure 6c shows the time-dependent fluorescence signal intensity for different quantum dot concentrations for the same number of beads. First, we injected a blank sample which does not contain any fluorescence tag but just the bead. The signal trace for 0 nM sample shown in black which does not show any rise in output current of the detector. The fluctuation for the 0 nM sample is around 0.25–0.65 nA which is due to the internal noise, scattered, and the background light. Then, we injected 50, 100, 500, and 1000 nM samples one by one at a flow rate of 30 $\mu\text{L}/\text{h}$ resulting in a sharp rise and decay when we turn the excitation light on and off, respectively. As the increase of sample concentration increases the fluorescence signal, the output current increases proportionally, as shown in Figure 6c, which signifies the excellent detecting capability of the perovskite detector. The maximum output current from the fluorescence when the excitation light is on was recorded as 1.153, 1.521, 1.960, and 2.204 nA for 50, 100, 500, and 1000 nM, respectively.

Then, we generated the calibration curve, as shown in Figure 6d. The data were collected three times to determine the mean and the standard deviation. The calibration curve initially starts to rise linearly up to 100 nM but then saturates as the concentration increases. The saturation observed in the calibration curve beyond 100 nM is attributed to the limited surface area of the beads, which restricts the number of available binding sites for the quantum dots or analyte. As the concentration increases, these binding sites gradually become fully occupied, resulting in a saturation in fluorescence intensity. The fluorescence intensity obtained for similar quantum dot concentrations using flow cytometer is provided in the Supporting Information in Figure S6 for a comparison which matches closely further validates the capability of our

perovskite detector. Finally, we determined the limit of detection focusing on the linear portion of the calibration curve. The slope and the R^2 value for the linear regression line were calculated to be 0.011 and 0.969, respectively. We then repeated the experiment for the blank sample five times to determine the standard deviation. The limit of detection was calculated as 23 nM by multiplying the standard deviation of the blank by 3 and then divided by the slope of the calibration curve. This result is very promising and could facilitate further research utilizing this perovskite-based detector for real sample measurement as the clinical concentration range for glucose detection is approximately 3.9–11.1 mM in human blood, and the relevant range for lactate is 0.5–2.2 mM for healthy individuals.

CONCLUSIONS

In this work, we have demonstrated the potential of the CsPbBr_3I perovskite-based photodetector for self-powered operation and optofluidic integration. By harnessing the controlled light-induced poling phenomenon, an electric field was induced within the perovskite material, eliminating the stability and degradation issues associated with traditional electrical poling methods. Our fabricated photodetector exhibited outstanding performance metrics, including an exceptionally low dark current, a high on/off ratio, notable responsivity, impressive detectivity, high dynamic range, and fast response time, all at 0 V. These promising results led us to explore its practical applications by integrating this photodetector with a microfluidic chip, highlighting its applicability in biomedical fields, particularly for the detection of fluorescently tagged microparticles. This could accelerate further research into self-powered fluorescence-based biomarker monitoring by integrating with other nano/micro devices within biological platforms.

ASSOCIATED CONTENT

Supporting Information

The Supporting Information is available free of charge at <https://pubs.acs.org/doi/10.1021/acsaem.4c01735>.

Microfluidic chip design, integrated optofluidic setup, elemental analysis by SEM-EDS mapping, Tauc plot, photocurrent stability study, and flow cytometry data plot ([PDF](#))

AUTHOR INFORMATION

Corresponding Authors

Vivek Maheshwari – Department of Chemistry, Waterloo Institute for Nanotechnology, University of Waterloo, Waterloo, ON N2L 3G1, Canada; Email: vmaheshwari@uwaterloo.ca

Dayan Ban – Department of Electrical and Computer Engineering, Waterloo Institute for Nanotechnology, University of Waterloo, Waterloo, ON N2L 3G1, Canada; Email: dban@uwaterloo.ca

Authors

Md Fahim Al Fattah – Department of Electrical and Computer Engineering, Waterloo Institute for Nanotechnology, University of Waterloo, Waterloo, ON N2L 3G1, Canada; orcid.org/0000-0002-5655-4534

Asif Abdullah Khan — Department of Electrical and Computer Engineering, Waterloo Institute for Nanotechnology, University of Waterloo, Waterloo, ON N2L 3G1, Canada

Saikiran Khamgaonkar — Department of Chemistry, Waterloo Institute for Nanotechnology, University of Waterloo, Waterloo, ON N2L 3G1, Canada

Sanjana Srikant — Department of Electrical and Computer Engineering, Waterloo Institute for Nanotechnology, University of Waterloo, Waterloo, ON N2L 3G1, Canada

Hesam Abouali — Department of Electrical and Computer Engineering, Waterloo Institute for Nanotechnology, University of Waterloo, Waterloo, ON N2L 3G1, Canada

Md. Rasidul Islam — Department of Electrical and Electronic Engineering, Bangamata Sheikh Fojilatunnesa Mujib Science & Technology University, Jamalpur 2012, Bangladesh;

 orcid.org/0000-0002-9916-793X

Aixi Pan — Department of Electrical and Computer Engineering, Waterloo Institute for Nanotechnology, University of Waterloo, Waterloo, ON N2L 3G1, Canada

Mohsen Azadinia — Department of Electrical and Computer Engineering, Waterloo Institute for Nanotechnology, University of Waterloo, Waterloo, ON N2L 3G1, Canada

Md. Soyaeb Hasan — Department of Electrical and Computer Engineering, Waterloo Institute for Nanotechnology, University of Waterloo, Waterloo, ON N2L 3G1, Canada

Mahmoud Almadhoun — Department of Electrical and Computer Engineering, Waterloo Institute for Nanotechnology, University of Waterloo, Waterloo, ON N2L 3G1, Canada

Hany Aziz — Department of Electrical and Computer Engineering, Waterloo Institute for Nanotechnology, University of Waterloo, Waterloo, ON N2L 3G1, Canada;

 orcid.org/0000-0002-5973-4979

Mahla Poudineh — Department of Electrical and Computer Engineering, Waterloo Institute for Nanotechnology, University of Waterloo, Waterloo, ON N2L 3G1, Canada;

 orcid.org/0000-0001-8684-3102

Complete contact information is available at:

<https://pubs.acs.org/10.1021/acsaem.4c01735>

Author Contributions

#M.F.A.F. and A.A.K. contributed equally. M.F.A.F. and A.A.K. conceived the main idea, collected and analyzed the data, and wrote the manuscript. S.K. helped with the device fabrication. S.S. prepared the biological sample. H.A. fabricated the microfluidic chip. M.R.R. simulated the band structure. A.P. helped with the SEM image collection. All other authors discussed the results, edited, and approved the manuscript.

Funding

D.B. acknowledges the financial support from Natural Sciences and Engineering Research Council of Canada (NSERC) Alliance grant. V.M. acknowledges financial support from NSERC, CFI, and the University of Waterloo.

Notes

The authors declare no competing financial interest.

ACKNOWLEDGMENTS

The authors acknowledge the experimental supports from Quantum-Nano Fabrication and Characterization Facility (QNFCF) and Giga-to-Nano Electronics (G2N) lab at the University of Waterloo, Canada. The authors also acknowledge the experimental help from Edward H. Sargent group.

REFERENCES

- (1) Sheng, X.; Gao, L.; Song, Y. M.; Tao, H.; Yun, S. H. Bio-inspired and bio-integrated photonic materials and devices: feature issue introduction. *Opt. Mater. Express* **2020**, *10*, 155–156.
- (2) Xu, H.; Yin, L.; Liu, C.; Sheng, X.; Zhao, N. Recent advances in biointegrated optoelectronic devices. *Adv. Mater.* **2018**, *30*, No. 1800156.
- (3) Sulaman, M.; Yang, S.; Guo, H.; Li, C.; Imran, A.; Bukhtiar, A.; Qasim, M.; Ge, Z.; Song, Y.; Jiang, Y.; Zou, B. Synergistic enhancement of CsPbI₃ nanorod-based high-performance photodetectors via PbSe quantum dot interface engineering. *Chem. Sci.* **2024**, *15*, 8514–8529.
- (4) Shen, K.; Xu, H.; Li, X.; Guo, J.; Sathasivam, S.; Wang, M.; Ren, A.; Leong Choy, K.; Parkin, I. P.; Guo, Z.; Wu, J. Flexible and self-powered photodetector arrays based on all-inorganic CsPbBr₃ quantum dots. *Adv. Mater.* **2020**, *32*, No. 2000004.
- (5) Fattah, M. F. A.; Khan, A. A.; Anabestani, H.; Rana, M. M.; Rassel, S.; Therrien, J.; Ban, D. Sensing of ultraviolet light: a transition from conventional to self-powered photodetector. *Nanoscale* **2021**, *13*, 15526.
- (6) Yun, S. H.; Kwok, S. J. J. Light in diagnosis, therapy and surgery. *Nat. Biomed. Eng.* **2017**, *1*, No. 0008.
- (7) Rogers, J. A. Electronics for the human body. *JAMA* **2015**, *313*, 561–562.
- (8) Zhu, H. L.; Xiao, J.; Mao, J.; Zhang, H.; Zhao, Y.; Choy, W. C. H. Controllable crystallization of CH₃NH₃Sn_{0.25}Pb_{0.75}I₃ perovskites for hysteresis-free solar cells with efficiency reaching 15.2%. *Adv. Funct. Mater.* **2017**, *27*, No. 1605469.
- (9) Shrestha, S.; Fischer, R.; Matt, G. J.; Feldner, P.; Michel, T.; Osvet, A.; Levchuk, I.; Merle, B.; Golkar, S.; Chen, H.; Tedde, S. F.; Schmidt, O.; Hock, R.; Rührig, M.; Göken, M.; Heiss, W.; Anton, G.; Brabec, C. J. High-performance direct conversion x-ray detectors based on sintered hybrid lead triiodide perovskite wafers. *Nat. Photonics* **2017**, *11*, 436.
- (10) Zhu, H. L.; Liang, Z.; Huo, Z.; Ng, W. K.; Mao, J.; Wong, K. S.; Yin, W. J.; Choy, W. C. Low-bandgap methylammonium-rubidium cation Sn-rich perovskites for efficient ultraviolet–visible–near infrared photodetectors. *Adv. Funct. Mater.* **2018**, *28*, No. 1706068.
- (11) Wang, Y.; Li, X.; Song, J.; Xiao, L.; Zeng, H.; Sun, H. All-inorganic colloidal perovskite quantum dots: a new class of lasing materials with favorable characteristics. *Adv. Mater.* **2015**, *27*, 7101.
- (12) Lin, H.; Zhu, L.; Huang, H.; Reckmeier, C. J.; Liang, C.; Rogach, A. L.; Choy, W. C. H. Efficient near-infrared light-emitting diodes based on organometallic halide perovskite–poly (2-ethyl-2-oxazoline) nanocomposite thin films. *Nanoscale* **2016**, *8*, 19846.
- (13) Mei, L.; Huang, R.; Shen, C.; Hu, J.; Wang, P.; Xu, Z.; Huang, Z.; Zhu, L. Hybrid halide perovskite-based near-infrared photodetectors and imaging arrays. *Adv. Opt. Mater.* **2022**, *10*, No. 2102656.
- (14) Hao, F.; Stoumpos, C. C.; Chang, R. P. H.; Kanatzidis, M. G. Anomalous band gap behavior in mixed Sn and Pb perovskites enables broadening of absorption spectrum in solar cells. *J. Am. Chem. Soc.* **2014**, *136*, 8094.
- (15) Stoumpos, C. C.; Malliakas, C.; Kanatzidis, M. G. Semiconducting tin and lead iodide perovskites with organic cations: phase transitions, high mobilities, and near-infrared photoluminescent properties. *Inorg. Chem.* **2013**, *52*, 9019.
- (16) Sulaman, M.; Song, Y.; Yang, S.; Li, M.; Saleem, M. I.; Chandrasekar, P. V.; Jiang, Y.; Tang, Y.; Zou, B. Ultra-sensitive solution-processed broadband photodetectors based on vertical field-effect transistor. *Nanotechnology* **2020**, *31*, 105203.
- (17) Sulaman, M.; Yang, S.; Jiang, Y.; Tang, Y.; Zou, B. Enhanced performance of solution-processed broadband photodiodes by epitaxially blending MAPbBr₃ quantum dots and ternary PbS_xSe_{1-x} quantum dots as the active layer. *Nanotechnology* **2017**, *28*, 505501.
- (18) Dong, H.; Ran, C.; Gao, W.; Li, M.; Xia, Y.; Huang, W. Metal halide perovskite for next-generation optoelectronics: progresses and prospects. *ELight* **2023**, *3*, 3.
- (19) Georgiadou, D. G.; Lin, Y. H.; Lim, J.; Ratnasingham, S.; McLachlan, M. A.; Snaith, H. J.; Anthopoulos, T. D. High responsivity

- and response speed single-layer mixed-cation lead mixed-halide perovskite photodetectors based on nanogap electrodes manufactured on large. *Adv. Funct. Mater.* **2019**, *29*, No. 1901371.
- (20) Sulaman, M.; Song, Y.; Yang, S.; Hao, Q.; Zhao, Y.; Li, M.; Saleem, M. I.; Chandrasekar, P. V.; Jiang, Y.; Tang, Y.; Zou, B. High-performance solution-processed colloidal quantum dots-based tandem broadband photodetectors with dielectric interlayer. *Nanotechnology* **2019**, *30*, 465203.
- (21) Miyasaka, T.; Kulkarni, A.; Kim, G.; Öztürk, S.; Jena, A. K. Perovskite solar cells: can we go organic-free, lead-free, and dopant-free? *Adv. Energy Mater.* **2020**, *10*, No. 1902500.
- (22) Zhang, H.; Jin, Z. Suppressed light-induced phase transition of CsPbBr₂I: strategies, progress and applications in the photovoltaic field. *J. Semicond.* **2021**, *42*, No. 071901.
- (23) Duan, J.; Zhao, Y.; He, B.; Tang, Q. High-purity inorganic perovskite films for solar cells with 9.72% efficiency. *Angew. Chem., Int. Ed.* **2018**, *57*, 3787.
- (24) Wang, X.; Wang, Y.; Chen, Y.; Liu, X.; Zhao, Y. Efficient and stable CsPbI₃ inorganic perovskite photovoltaics enabled by crystal secondary growth. *Adv. Mater.* **2021**, *33*, No. 2103688.
- (25) Zhang, B.; Bi, W.; Wu, Y.; Chen, C.; Li, H.; Song, Z.; Dai, Q.; Xu, L.; Song, H. High-performance CsPbIBr₂ perovskite solar cells: effectively promoted crystal growth by antisolvent and organic ion strategies. *ACS Appl. Mater. Interfaces* **2019**, *11*, 33868.
- (26) Sun, J.; Zhao, X.; Si, H.; Gao, F.; Zhao, B.; Ouyang, T.; Li, Q.; Liao, Q.; Zhang, Y. Defect passivation and energy level modulation of CsPbBr₂I QDs for high-detectivity and stable photodetectors. *Adv. Opt. Mater.* **2023**, *11*, No. 2202877.
- (27) Pang, T.; Jia, R.; Wang, Y.; Sun, K.; Hu, Z.; Zhu, Y.; Luan, S.; Zhang, Y. Self-powered behavior based on the light-induced self-poling effect in perovskite-based transport layer-free photodetectors. *J. Mater. Chem. C* **2019**, *7*, 609.
- (28) Yuan, Y.; Huang, J. Ion migration in organometal trihalide perovskite and its impact on photovoltaic efficiency and stability. *Acc. Chem. Res.* **2016**, *49*, 286.
- (29) Zhu, X.; Lee, J.; Lu, W. D. Iodine vacancy redistribution in organic–inorganic halide perovskite films and resistive switching effects. *Adv. Mater.* **2017**, *29*, No. 1700527.
- (30) Yuan, Y.; Wang, Q.; Shao, Y.; Lu, H.; Li, T.; Gruverman, A.; Huang, J. Electric-field-driven reversible conversion between methylammonium lead triiodide perovskites and lead iodide at elevated temperatures. *Adv. Energy Mater.* **2016**, *6*, No. 1501803.
- (31) Chen, X.; Han, D.; Su, Y.; Zeng, Q.; Liu, L.; Shen, D. Structural and electronic properties of inorganic mixed halide perovskites. *Phys. Status Solidi RRL* **2018**, *12*, No. 1800193.
- (32) Tran, F.; Blaha, P. Accurate band gaps of semiconductors and insulators with a semilocal exchange-correlation potential. *Phys. Rev. Lett.* **2009**, *102*, No. 226401.
- (33) Fattah, M. F. A.; Amin, M. R.; Mallmann, M.; Kasap, S.; Schnick, W.; Moewes, A. Electronic structure investigation of wide band gap semiconductors - Mg₂PN₃ and Zn₂PN₃: experiment and theory. *J. Phys.: Condens. Matter* **2020**, *32*, 405504.
- (34) Perdew, J. P.; Burke, K.; Ernzerhof, M. Generalized gradient approximation made simple. *Phys. Rev. Lett.* **1996**, *77*, 3865.
- (35) Li, J.; Wang, J.; Ma, J.; Shen, H.; Li, L.; Duan, X.; Li, D. Self-trapped state enabled filterless narrowband photodetections in 2d layered perovskite single crystals. *Nat. Commun.* **2019**, *10*, 806.
- (36) Liu, D.; Yu, B.; Bin; Liao, M.; Jin, Z.; Zhou, L.; Zhang, X.; Wang, F.; He, H.; Gatti, T.; He, Z. Self-powered and broadband lead-free inorganic perovskite photodetector with high stability. *ACS Appl. Mater. Interfaces* **2020**, *12*, 30530.
- (37) Lin, L.; Liu, Y.; Wu, W.; Huang, L.; Zhu, X.; Xie, Y.; Liu, H.; Zheng, B.; Liang, J.; Sun, X.; Zhu, C.; Wu, G.; Shuai, Q.; Huang, Z.; Wang, T.; Li, D.; Pan, A. Self-powered perovskite photodetector arrays with asymmetric contacts for imaging applications. *Adv. Electron. Mater.* **2023**, *9*, No. 2300106.
- (38) Hussain, A. A. Constructing caesium-based lead-free perovskite photodetector enabling self-powered operation with extended spectral response. *ACS Appl. Mater. Interfaces* **2020**, *12*, 46317.
- (39) Pan, X.; Zhou, H.; Liu, R.; Wu, D.; Song, Z.; Tang, X.; Yang, X.; Wang, H. Achieving a high-performance, self-powered, broadband perovskite photodetector employing MAPbI₃ microcrystal films. *J. Mater. Chem. C* **2020**, *8*, 2028.
- (40) Liang, F. X.; Zhou, L. L.; Hu, Y.; Li, S. F.; Zhang, Z. Y.; Li, J. Y.; Fu, C.; Wu, C. Y.; Wang, L.; Huang, J. A.; Luo, L. B. Self-driven narrow-band photodetector based on FAPbBr_{2.5}I_{0.5} single crystal for yellow light intensity meter application. *Adv. Funct. Mater.* **2023**, *33*, No. 2302175.
- (41) Li, C.; Han, C.; Zhang, Y.; Zang, Z.; Wang, M.; Tang, X.; Du, J. Enhanced photoresponse of self-powered perovskite photodetector based on ZnO nanoparticles decorated CsPbBr₃ films. *Sol. Energy Mater. Sol. Cells* **2017**, *172*, 341.
- (42) Yang, B.; Zhang, F.; Chen, J.; Yang, S.; Xia, X.; Pullerits, T.; Deng, W.; Han, K. Ultrasensitive and fast all-inorganic perovskite-based photodetector via fast carrier diffusion. *Adv. Mater.* **2017**, *29*, No. 1703758.
- (43) Cao, F.; Meng, L.; Wang, M.; Tian, W.; Li, L. Gradient energy band driven high-performance self-powered perovskite/CdS photodetector. *Adv. Mater.* **2019**, *31*, No. 1806725.
- (44) Deng, H.; Yang, X.; Dong, D.; Li, B.; Yang, D.; Yuan, S.; Qiao, K.; Cheng, Y. B.; Tang, J.; Song, H. Flexible and semitransparent organolead triiodide perovskite network photodetector arrays with high stability. *Nano Lett.* **2015**, *15*, 7963.
- (45) Sun, H.; Lei, T.; Tian, W.; Cao, F.; Xiong, J.; Li, L. Self-powered, flexible, and solution-processable perovskite photodetector based on low-cost carbon cloth. *Small* **2017**, *13*, No. 1701042.
- (46) Saidaminov, M. I.; Haque, M. A.; Almutlaq, J.; Sarmah, S.; Miao, X. H.; Begum, R.; Zhumekenov, A. A.; Dursun, I.; Cho, N.; Murali, B.; Mohammed, O. F.; Wu, T.; Bakr, O. M. Inorganic lead halide perovskite single crystals: phase-selective low-temperature growth, carrier transport properties, and self-powered photodetection. *Adv. Opt. Mater.* **2017**, *5*, No. 1600704.
- (47) Shafique, S.; Qadir, A.; Iqbal, T.; Sulaman, M.; Yang, L.; Hou, Y.; Miao, Y.; Wu, J.; Wang, Y.; Zheng, F.; Wang, X.; Hu, Z. High-performance self-powered perovskite photodetectors enabled by Nb₂CT_x-passivated buried interface. *J. Alloys Compd.* **2024**, *1004*, No. 175903.
- (48) Sulaman, M.; Yang, S.; Imran, A.; Zhang, Z.; Bukhtiar, A.; Ge, Z.; Song, Y.; Sun, F.; Jiang, Y.; Tang, L.; Zou, B. Two bulk-heterojunctions made of blended hybrid nanocomposites for high-performance broadband, self-driven photodetectors. *ACS Appl. Mater. Interfaces* **2023**, *15*, 25671–25683.
- (49) Sulaman, M.; Yang, S. Y.; Zhang, Z. H.; Imran, A.; Bukhtiar, A.; Ge, Z. H.; Tang, Y.; Jiang, Y. R.; Tang, L. B.; Zou, B. S. Lead-free tin-based perovskites nanocrystals for high-performance self-driven bulk-heterojunction photodetectors. *Mater. Today Phys.* **2022**, *27*, No. 100829.
- (50) Sulaman, M.; Sulaman, M.; Song, Y.; Yang, S.; Yang, S.; Saleem, M. I.; Li, M.; Perumal Veeramalai, C.; Zhi, R.; Jiang, Y.; Cui, Y.; Hao, Q.; Zou, B. Interlayer of PMMA doped with Au nanoparticles for high-performance tandem photodetectors: A solution to suppress dark current and maintain high photocurrent. *ACS Appl. Mater. Interfaces* **2020**, *12*, 26153–26160.
- (51) Sulaman, M.; Yang, S.; Bukhtiar, A.; Tang, P.; Zhang, Z.; Song, Y.; Imran, A.; Jiang, Y.; Cui, Y.; Tang, L.; Zou, B. Hybrid bulk-heterojunction of colloidal quantum dots and mixed-halide perovskite nanocrystals for high-performance self-powered broadband photodetectors. *Adv. Funct. Mater.* **2022**, *32*, No. 2201527.
- (52) Poudineh, M.; Maikawa, C. L.; Ma, E. Y.; Pan, J.; Mamerow, D.; Hang, Y.; Baker, S. W.; Beirami, A.; Yoshikawa, A.; Eisenstein, M.; Kim, S.; Vučković, J.; Appel, E. A.; Soh, H. T. A fluorescence sandwich immunoassay for the real-time continuous detection of glucose and insulin in live animals. *Nat. Biomed. Eng.* **2021**, *5*, 53.
- (53) Psaltis, D.; Quake, S. R.; Yang, C. Developing optofluidic technology through the fusion of microfluidics and optics. *Nature* **2006**, *442*, 381.
- (54) Schmidt, H.; Hawkins, A. R. The photonic integration of non-solid media using optofluidics. *Nat. Photonics* **2011**, *5*, 598.

(55) Fattah, M. F. A.; Abouali, H.; Hosseini, S. A.; Yin, J.; Khan, A. A.; Aghamohammadi, H.; Poudineh, M.; Ban, D. An optofluidic system for monitoring fluorescently activated protein biomarkers. *Anal. Sens.* **2023**, *4*, No. e202300064.

(56) Schmidt, O.; Bassler, M.; Kiesel, P.; Koos, C. Fluorescence spectrometer-on-a-fluidic-chip. *Lab Chip* **2007**, *7*, 626.

(57) Li, Q.; Cui, S.; Xu, Y.; Wang, Y.; Jin, F.; Si, H.; Li, L.; Tang, B. Consecutive sorting and phenotypic counting of CTCs by an optofluidic flow cytometer. *Anal. Chem.* **2019**, *91*, 14133.